Thermographic Detection of Fatigue Damage of Reactor Pressure Vessel (RPV) Steels

Bing Yang

(Submitted 4 February 2003; in revised form 19 February 2003)

An IR (IR) thermography technique, as a nondestructive evaluation technique, was applied to investigate the fatigue damage of reactor pressure vessel (RPV) steels during 20 Hz and 1000 Hz fatigue testing. Five stages of temperature profile were observed: an initial increase of the average specimen temperature, a region of temperature decrease, an equilibrium (steady-state) temperature region, an abrupt increase of the temperature, and a drop of temperature following specimen failure. The relationship between the temperature, stress-strain state, and fatigue behavior is discussed. Both thermodynamic and heat-transfer theories are applied to model the observed temperature variation during fatigue. The stress-strain state of the material has been back-calculated from the observed temperature profiles. The predicted and measured temperature evolutions and mechanical behavior during fatigue were found to be in good agreement. Thermography appears to provide a useful method of investigating the stress-strain behavior during fatigue.

Keywords fatigue, nondestructive evaluation, RPV steel, temperature evolution, thermography

1. Introduction

In 1829, the first fatigue test was performed in Germany on steel chains, which were subjected to 100 000 tension cycles at a frequency of 10 cycles per minute. Since then, a great amount of valuable research has examined the fatigue behavior of materials due to the irreplaceable significance of this subject in the engineering world.[1-8] In recent decades, fracture mechanics has become the dominant concept used in describing and understanding fatigue behavior.

Although there is still excitement about concepts like fracture toughness and endurance limit, data scattering, time-consuming and costly experiments can give some difficulties during fatigue testing of industrial components and structures. Thus, more and more efforts have been focused on nondestructive evaluation (NDE) techniques for their critical importance in fatigue-life assessments, structural-integrity evaluations, failure prevention, and material savings. Several NDE methods have been applied to monitor mechanical damage, including ultrasonics, acoustic emission, eddy current, x-ray, and computed tomography,[9-12] but relatively little work has been done to characterize the fatigue behavior using thermographic IR (IR) techniques.[13-17]

The relationship between material deformation and temperature was first recognized in 1853 by Kelvin.[18] The thermoelastic[18-20] and inelastic[21] effects directly relate the temperature to the material internal stress-strain state, which, in turn, controls the fatigue behavior. However, the limited sensitivity of the available instrumentation has restrained the full development of thermography as an NDE technique until the last two decades.[22-24] Recently, more research has shown the potential of thermography in monitoring fatigue damage.[25-27] Methods for the short-time measurement of fatigue limits have also been suggested.[28] However, detailed investigations and comprehensive analyses are necessary for developing an effective thermographic technique in characterizing fatigue behavior, and detecting the associated damage.

In this paper, an advanced high-frequency and high-sensitivity IR imaging system was used to monitor the temperature evolution of reactor pressure vessel steels subjected to 20 Hz and 1000 Hz fatigue tests. Both thermodynamics and heat-conduction theories are applied to explain and model the observed temperature evolutions during fatigue.

2. Experimental Procedure

2.1 Material

The material used in fatigue tests is a reactor pressure vessel (RPV) steel (SA533B1I2), which is composed of 0.203C, 0.23Si, 1.34Mn, <0.02P, 0.015S, 0.50Ni, 0.53Mo, 0.15Al, 0.005N, 0.01Cu, and balance Fe (wt.%). The steel plate was first solution-treated at 899 °C for 1 h, then water-quenched to 40 °C, and finally tempered at 670 °C for 1 h. A tempered martensite was the final microstructure. The yield strength of the RPV steel was 587 MPa, ultimate tensile strength (UTS) was 716 MPa, and total elongation was 29%, with a strain rate of 4×10^{-3}/s and a gage length of 1.27 cm used in the tension test. A yielding phenomenon was observed in the test, as discussed later.

2.2 Fatigue Testing

Fatigue test samples are cylindrical bars with a gage length of 1.27 cm and a diameter of 0.508 cm at the gage section. The test samples are machined from the steel plate with the length direction parallel to the rolling direction, and then polished in

Bing Yang, Department of Materials Science and Engineering, University of Tennessee, Knoxville, TN 37996-2200. Contact e-mail: byang@utk.edu.

a sequence of 240, 400, 600, and 800 grit papers, followed by 9.5, 1, and 0.06 μm Al_2O_3 grit powders.

The 1000 Hz fatigue tests were performed using an advanced high-frequency electrohydraulic MTS (Material Test System, Eden Praire, MN) machine (Model 1,000 Hz 810) with an R ratio of 0.2, where $R = \sigma_{min}/\sigma_{max}$, σ_{min}, and σ_{max} are the applied minimum and maximum stresses, respectively.[29] The servovalves of the machine were activated by voice coils, which provided the necessary frequency of 1000 Hz.

For the 20 Hz fatigue experiments in air, the specimens were loaded on an MTS machine (Model 810) at R = 0.2. A load control mode was used, and different maximum stress levels ranging from 500-650 MPa were applied.

2.3 Thermography

Thermography detection was conducted using a state-of-the-art Raytheon Galileo thermographic IR (IR) imaging system (Indigo Systems Corp., Goleta, CA) with a 256 × 256 pixels focal-plane-array InSb detector that is sensitive to a radiation wavelength of 3-5 μm. The temperature sensitivity is 0.015 °C at 23 °C, while the spatial resolution can be as small as 5.4 μm. The system has a maximum data acquisition speed of 150 Hz at a full frame of 256 × 256 pixels and 6100 Hz at 16 × 16 pixels. During fatigue testing, a thin sub-micron graphite coating was applied on the specimen gage-length section to decrease surface-heat reflection.

A thermocouple was attached to the sample to calibrate the IR camera at the beginning of each test. During calibration, a heat gun was first used to heat up the specimen to a high temperature. The specimen was then cooled in air, and the temperature of the specimen was recorded from the thermocouple at different times. Then, the intensity of the IR camera was calibrated to the corresponding temperature. A fully automated software system was used to acquire the data of temperature distributions of the test samples during fatigue experiments. The IR camera was used at low scan frequency of 0.1 and 0.2 Hz, and a high scan frequency of 120 Hz.

3. Results and Discussion

3.1 Fatigue Life and Temperature Evolution

The S (applied stress) versus N (fatigue life cycle) curves of RPV steels at 1000 Hz and 20 Hz are presented in Fig. 1. Increasing the test frequency from 20 Hz to 1000 Hz generally resulted in a shorter fatigue life. Specifically, the fatigue endurance limit at 20 Hz seems to be higher than that at 1000 Hz. Thermography detection results show that during fatigue testing, the temperature evolution at 1000 Hz (Fig. 2) is much higher than that at 20 Hz (Fig. 3), which could contribute to the lower fatigue life at 1000 Hz than at 20 Hz. The details of the temperature profiles have been discussed in previous work.[26]

The temperature profile (Fig. 3) was plotted in Fig. 4 on a log scale of fatigue cycles for the 20 Hz fatigue test with an R ratio of 0.2 and maximum stress level of 640 MPa. The temperature profile in Fig. 4 was recorded at the midpoint of the specimen gage-length section using the IR camera at a high speed of 120 Hz (compared with a low speed of 0.1 Hz used in Fig. 3). In Fig. 4, an initial increase in the temperature from 23.7-28.5 °C, followed by a temperature decrease (i.e., a temperature hump) in the first 100 cycles, was observed, which did not show up in Fig. 3 due to the lower camera speed, compared with Fig. 4. Also, 100 cycles are too short to be noticed on a normal scale in Fig. 3. After the hump, the temperature approached a steady state of about 27 °C due to the thermal equilibrium between the specimen and the environment. Next, the temperature increased abruptly from approximately 27-46 °C until the specimen broke due to the heat from the large plastic deformation at the crack tip. Following that, the sample failed, and the temperature dropped.

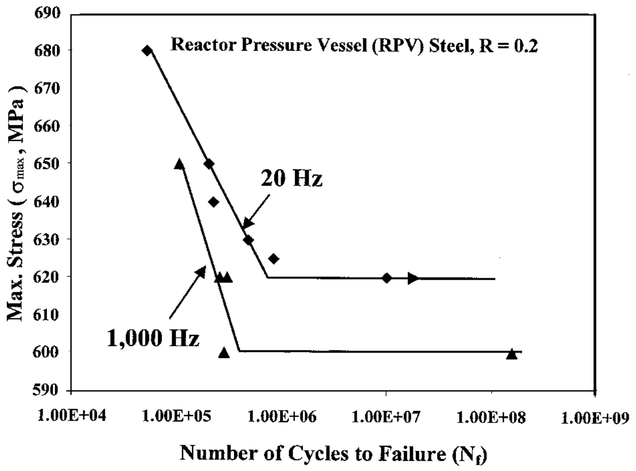

Fig. 1 Fatigue results of reactor pressure vessel steel

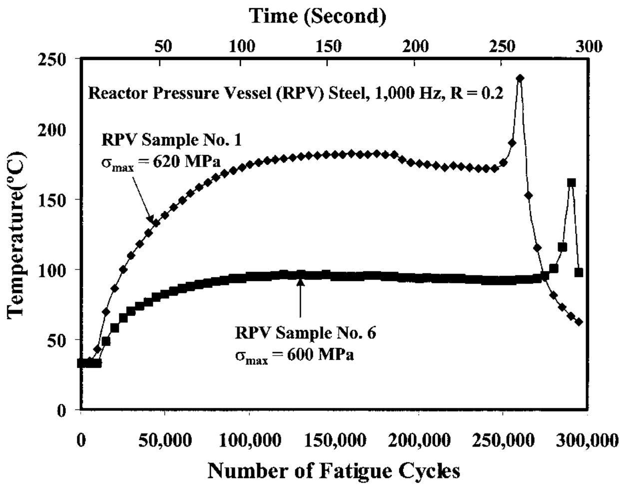

Fig. 2 Temperature profile of reactor pressure vessel steel during 1000 Hz fatigue testing, taken at an IR camera speed of 0.2 Hz

3.2 Temperature Hump

In Fig. 5, the dashed line represents the amplified hump in Fig. 4. In Fig. 5, at the first stage, a slight temperature decrease within the first 0.7 s is due to the thermoelastic effect, as discussed later. Then, the temperature rose rapidly from the first fatigue cycle at approximately 0.7 s and a temperature of

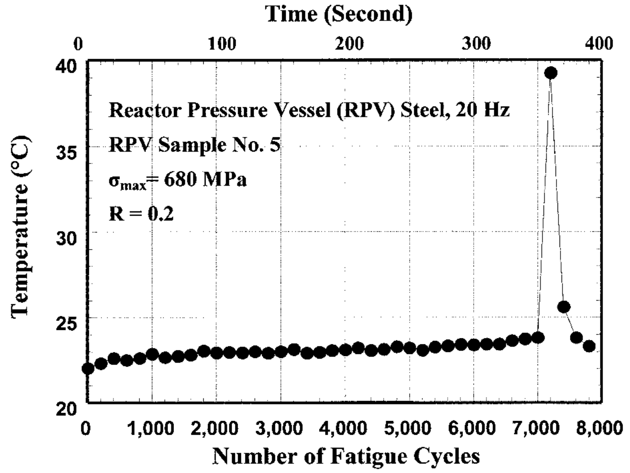

Fig. 3 Temperature profile of reactor pressure vessel steel during 20 Hz fatigue testing, taken at an IR camera speed of 0.1 Hz

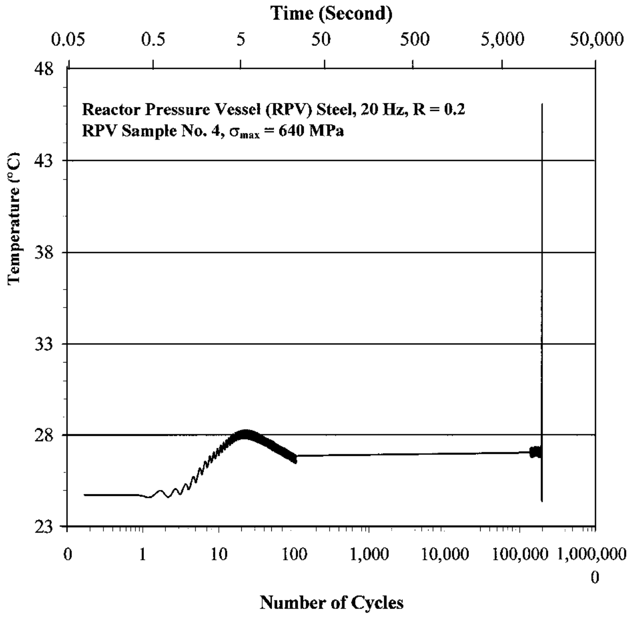

Fig. 4 Temperature profile of reactor pressure vessel steel during 20 Hz fatigue testing, taken at an IR camera speed of 120 Hz

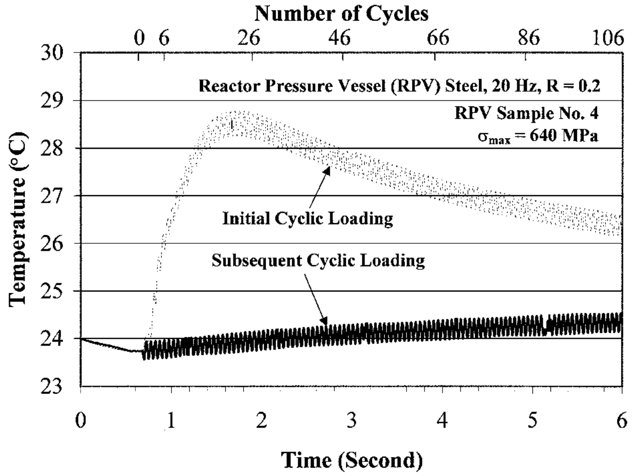

Fig. 5 Temperature versus time profiles of reactor pressure vessel steel tested at 20 Hz, σ_{max} = 640 MPa, taken at an Ir camera speed of 120 Hz

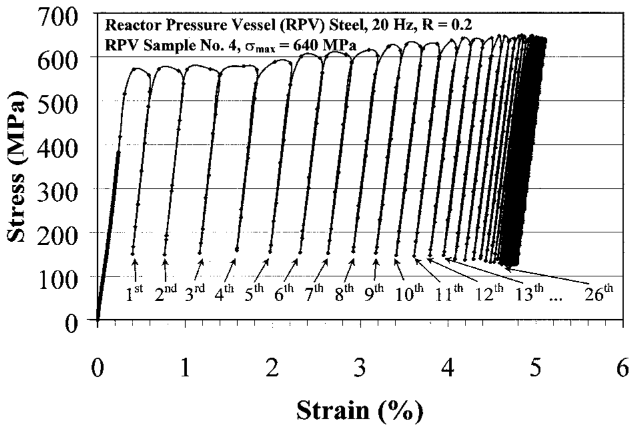

Fig. 6 Stress versus strain profiles of reactor stress versus strain tested at 20 Hz, σ_{max} = 640 MPa

23.7 °C, and reached a maximum of 28.5 °C at about 2 s. After that, the temperature decreased gradually to a relatively constant value. However, if the test was stopped after the temperature had become stable, and then restarted, no temperature hump was observed, and the corresponding results were plotted as a solid dark line in Fig. 5. Note that in both tests shown by the dashed and solid lines, temperature oscillations within the range of approximately less than 0.6 °C were observed within each fatigue cycle.

Since the mean temperature variation is closely related to the plastic deformation,[21,22] a reasonable explanation for the presence of the temperature hump can be obtained from the stress-strain curve in Fig. 6. This is a typical stress-strain curve for the tension-tension fatigue test. Corresponding to the temperature rise from approximately 0.7 s to 2 s in Fig. 5, the stress-strain curve in Fig. 6 moved from the first cycle to 26 cycles, and the plastic strain increased from 0 to nearly the saturated value of about 4.7%. During this period, a large amount of heat was generated from the large plastic deformation, and the temperature of the sample increased quickly. Moreover, the yielding phenomenon of RPV steels was observed in the uniaxial tensile test (Fig. 7), which contributed to large plastic (or inelastic) strains (Fig. 6), and, in turn, more heat was generated. However, after that (the first 26 cycles), relatively little plastic strain occurred due to the strain-hardening effect (Fig. 6), and the temperature decreased when the heat inside the sample was conducted to the environment, and finally reached a relatively constant value due to the thermal equilibrium between the heat generation of the specimen subjected to cyclic loading and the environment. Note that in Fig. 6, the maximum stress level was lower than 640 MPa for the first several cycles because the fatigue machine needs some time to stabilize the stress level at the beginning of the fatigue testing.

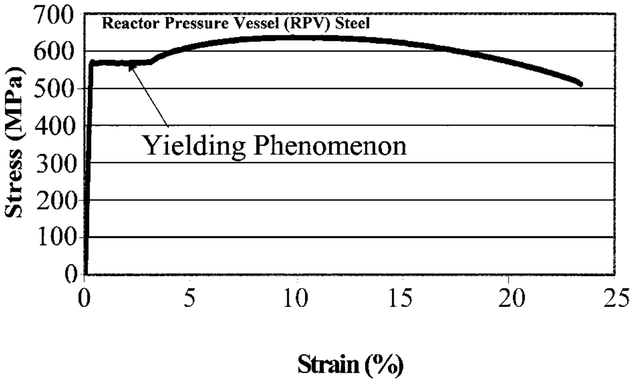

Fig. 7 Stress versus strain curve of reactor pressure vessel steel during tensile testing

If the fatigue test is terminated and restarted, little heat will be generated from the plastic deformation because the plastic strain has already saturated. Thus, there will be no rapid temperature rise in the first 100 cycles, as indicated by the solid lines in Fig. 5. This trend shows a good correspondence between the temperature evolutions and the stress-strain characteristics during fatigue.

4. Theoretical Modeling

Generally, in a fatigue test without outside heat sources, the variation of the specimen temperature can be explained by three factors[19-23]: (1) the thermoelastic effect, (2) the inelastic effect, and (3) the heat-conduction effect. Note that the thermoelastic effect contributes to the temperature oscillation, while the inelastic and heat-conduction effects play a dominant role in affecting the mean-temperature change.

In the following text, a model combining the thermoelastic, inelastic, and heat-conduction effects will be formulated. Specifically, the temperature profile during fatigue will be predicted and compared with the experimental data.

4.1 Thermoelastic Effect

During fatigue, the temperature was initially observed to decrease in an amount proportional to the increase of the stress in the ramp-up period, and then fluctuate regularly in a sinusoidal wave at the same frequency as the stress cycles (Fig. 5). The amplitude of the temperature oscillation is about 0.5 °C (Fig. 5). To explain these phenomena, a quantitative stress analysis by means of the thermoelastic effect needs to be developed.

The basic relationship among the entropy, temperature, and energy can be derived[18-20] from the laws of thermodynamics in the form:

$$ds = \frac{1}{T}\frac{\partial U}{\partial T}dT - \sum^{ij}\frac{\partial \sigma_{ij}}{\partial T}d\varepsilon_{ij} \quad \text{with } i, j = 1, 2, 3 \qquad \text{(Eq 1)}$$

where s is entropy, U is the internal energy, T is the absolute temperature, σ_{ij} is the stress component, and ε_{ij} is the strain component.

The basic equations of the stress, strain, and temperature are:

$$\sigma_{ij} = 2G\left(\varepsilon_{ij} + \frac{\nu}{1-2\nu}e\delta_{ij} - \frac{1+\nu}{1-2\nu}\alpha\Delta T\delta_{ij}\right) \qquad \text{(Eq 2)}$$

$$E = 2G(1+\nu) \qquad \text{(Eq 3)}$$

where G is the shear modulus, ν is Poisson's ratio, E is the Young's modulus, α is the coefficient of linear expansion, ΔT is the temperature change, ε_1, ε_2, and ε_3 are the principal strain components, $e = \varepsilon_1 + \varepsilon_2 + \varepsilon_3$, and $\delta_{ij} = \langle 1(i = j)|0(i \neq j)\rangle$.

Considering

$$\frac{\partial U}{\partial T} = \frac{\partial Q}{\partial T} = C_\varepsilon\rho,$$

where ρ is mass density and C_ε is the heat capacity at constant strain, and combining Eq 1-3, the following equation can be derived:

$$s = \frac{C_\varepsilon\rho\Delta T}{T} + \frac{E}{1-2\nu}(\varepsilon_1 + \varepsilon_2 + \varepsilon_3) \qquad \text{(Eq 4)}$$

where C_ε is the heat capacity under constant strain, and ρ is the density.

For a constant pressure,

$$Q = H = Ts = C_\varepsilon\rho\Delta T + \frac{ET}{1-2\nu}(\varepsilon_1 + \varepsilon_2 + \varepsilon_3) \qquad \text{(Eq 5)}$$

where Q is heat and H is the volumetric Helmholtz free energy.

The relationship between C_p, the heat capacity at a constant pressure, and C_ε is:

$$C_p - C_\varepsilon = \frac{3E\alpha^2T}{\rho(1-2\upsilon)} \qquad \text{(Eq 6)}$$

Combining Eq 2, 3, 5, and 6 gives:

$$Q = C_p\rho\Delta T + T\alpha(\sigma_1 + \sigma_2 + \sigma_3) \qquad \text{(Eq 7)}$$

where σ_1, σ_2, and σ_3 are the principal stress components.

Under adiabatic conditions, $Q = 0$,

$$\Delta T = -\frac{T\alpha}{C_p\rho}(\sigma_1 + \sigma_2 + \sigma_3) = -KT(\sigma_1 + \sigma_2 + \sigma_3) \qquad \text{(Eq 8)}$$

where K is the material constant, and equals

$$\frac{\alpha}{C_p\rho}$$

While the absolute temperature of the material does not change sharply during each fatigue cycle, the temperature will fluctuate in an amount proportional to the sum of the principal stresses, which has been observed in our uniaxial fatigue test.[30,31] In Eq 8, increasing the stress decreases the temperature, while decreasing the stress increases the temperature.[30,31]

4.2 Inelastic Effect

The thermoelastic effect, the heat from the plastic deformation, and the yielding phenomenon in Fig. 6 and 7 all contribute to the temperature-rise region of the hump during the first 100 fatigue cycles in Fig. 5 and 6. To quantify the heat-generation phenomenon of an elastic-plastic material during high-cycle fatigue, the following assumptions have been made:

1) Consider an isotropic, long, and slender bar, which is subjected to a homogeneously applied deformation field such that the resulting stress field is everywhere uniaxial in one dimension.
2) Only a fixed system of one-dimensional axis along the longitudinal direction of the cylindrical test bar will be considered.

Thus, considering only the plastic-strain contribution and neglecting the thermoelastic effect and thermal expansion, the basic thermodynamic equation[30] becomes:

$$\rho C_{\mathrm{p}} \frac{\partial T(x,t)}{\partial t} = k \frac{\partial^2 T(x,t)}{\partial x^2} + \Theta \qquad \text{(Eq 9)}$$

where Θ is the constant heat generation rate due to the inelastic deformation, k is the thermal conductivity, t is the time, x is the specimen gage-length dimension.

If considering only the thermoplastic effect, Eq 9 can be simplified to:

$$\rho C_{\mathrm{p}} \frac{\partial T(x,t)}{\partial t} = \Theta \qquad \text{(Eq 10)}$$

Since

$$W = \int \Theta dt = \int \sigma d\varepsilon,$$

where σ is the stress and ε is the strain, integrating Eq 10 with time gives:

$$\rho C_{\mathrm{p}} \theta_i = \int_{\varepsilon_{\min}}^{\varepsilon_{\max}} \sigma_u d\varepsilon - \int_{\varepsilon_{\min}}^{\varepsilon_{\max}} \sigma_l d\varepsilon = A_{\mathrm{i}} \qquad \text{(Eq 11)}$$

where θ is the temperature change due to the thermoplastic effect for each fatigue cycle, $\varepsilon_{\min}$ and $\varepsilon_{\max}$ are the minimum and maximum strains, respectively, of the hysteresis loop, σ_u and σ_l refer to the stresses in the upper and lower parts of the hysteresis loop, A is the area of each hysteresis loop, and i represents the number of each fatigue cycle.

4.3 Heat-Conduction Effect

To provide a better prediction of the thermography results, the heat-transfer effect needs to be considered. For RPV steels tested in air, two heat-transfer processes are involved. One is the heat conduction between the specimen and the main body of the MTS machine through grips and the other is the heat transfer between the specimen and the air around it. However, since the heat capacity of steel far exceeds that of air, it is reasonable to ignore the heat transfer to the air.

For steady one-dimensional conduction without energy conversion, the basic heat conduction equation is:

$$\rho C_{\mathrm{p}} \frac{\partial T}{\partial t} = k \frac{\partial^2 T}{\partial x^2} \qquad \text{(Eq 12)}$$

The specimen is held by a pair of grips that are loaded on the machine. For the continuity of the one-dimensional heat-conduction model, the length of the grips and non-gage section of the specimen need to be converted into an effective length of material with the same cross-sectional area as the gage section. The key is that the heat passing through a cross section should be the same before and after conversion. As for the inclusion of the heat-conduction effect, the temperature in the main body of the machine is equal to room temperature, and the length of the grips (20.32 mm) and non-gage length of the specimen (3.83 mm) are converted into an effective length of 14.05 mm with a diameter of 5.08 mm (the same as the gage diameter of the specimen).[31] Considering that the specimen is a homogeneous round bar, and assuming that the temperature gradient is constant with x-axis, a simplification can be made as follows:

$$\frac{\partial T}{\partial x} = \frac{T - T_0}{\Delta x} \qquad \text{(Eq 13)}$$

where T_0 is the room temperature of 24 °C, and Δx is the effective length from the center of the specimen to the end of the grip.

Since:

$$k \frac{\partial T^2}{\partial x^2} = k \frac{\partial \left(\frac{T - T_0}{\Delta x} \right)}{\partial x} = k \frac{1}{\Delta x} \frac{\partial T}{\partial x} \qquad \text{(Eq 14)}$$

Using Eq 13 and 14, Eq 12 can be converted into:

$$\frac{\partial T}{\partial t} = k \frac{1}{(\Delta x)^2 \rho C_{\mathrm{p}}} (T - T_0) \qquad \text{(Eq 15)}$$

In the following section, the thermoelastic, thermodynamic, and heat-transfer effects will be combined to predict the temperature evolutions versus the number of cycles curves, including the temperature variations in the first 100 cycles. The temperature evolutions will be predicted using the stress and strain data during fatigue cycles and compared with the experimental data.

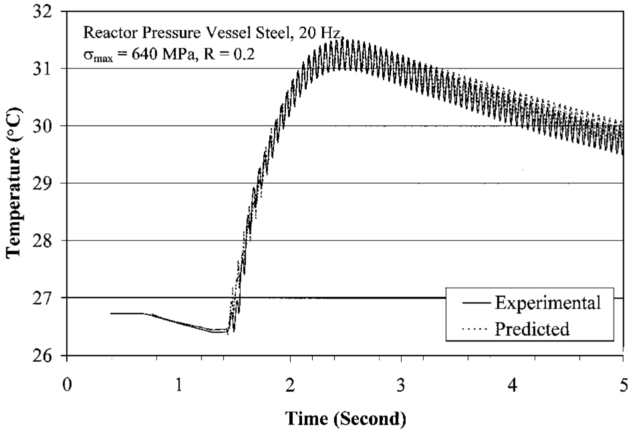

Fig. 8 Measured and predicted temperature evolutions of RPV steel during fatigue testing at 20 Hz, σ_{max} = 640 MPa

4.4 Comparisons of Experimental Results and Theoretical Predictions

The relevant material constants of the RPV steel are:

Linear thermal expansion coefficient: $\alpha = 1.1 \times 10^{-5}$ /°C
Density: $\rho = 7.8$ g/cm^3
Specific heat at a constant pressure: $C_p = 0.48$ J/g · °C
Thermal conductivity: $k = 50$ W/(m K)

Combining the calculation of the thermoelastic, inelastic, and heat-transfer effects using Eq 8, 11, and 15, the theoretical temperature profile of the whole temperature hump is predicted in Fig. 8. The detailed calculation has been given in Ref. 31. In this figure, the theoretical model predicts the temperature hump, which is in good agreement with the experimental data. However, the predictions and experimental results in the temperature-decrease part do not fit each other exactly. The deviation can be explained by the fact that the present heat-conduction model is a simplified model, while the real heat transfer between the specimen and environment is much more complicated (e.g., the heat transfer between the specimen and the surrounding air, and the temperature gradient not being exactly constant along the *x*-axis). Also, for the first two fatigue cycles, the predicted and measured results do not fit each other closely, which can be explained as follows. The surface and the center of the sample have not reached a uniform thermodynamic state at the very beginning of the test. The surface temperature can be more easily dissipated, relative to the interior of the sample. Thus, the measured surface temperatures of the test specimen by thermography can be lower than the predicted values.

4.5 Back Calculation

In the previous section, the prediction of the temperature profiles during fatigue has been conducted using the stress-strain data. In this section, the back calculation from the temperature to stress and strain state will be performed and thus the deformation behavior of RPV steels will be determined from thermography.

From the temperature profile in Fig. 5, we can easily calculate the stress state by the thermoelastic effect. At the ramp-up period of fatigue testing, the stress increases from zero to the mean stress of the fatigue testing. At the same time, the normalized temperature decreases from 24 °C to 23.67 °C (Fig. 5). The mean stress can then be calculated by Eq 8 as:

$$\left(\frac{\sigma_{max} + \sigma_{min}}{2}\right) = \frac{(T_1 - T_0)}{-KT_0} \qquad \text{(Eq 16)}$$

where σ_{max} and σ_{min} are the maximum and minimum stresses, respectively, and T_1 is the specimen temperature at the end of the ramp-up period, which equals to 23.67 °C.

At the constant temperature region, a temperature oscillation (ΔT_{osci}) of 0.46 °C can also be expressed by the equation below:

$$\Delta T_{osci} = -KT(\sigma_{max} - \sigma_{min}) \qquad \text{(Eq 17)}$$

Thus,

$$\left(\frac{\sigma_{max} - \sigma_{min}}{2}\right) = \frac{\Delta T_{osci}}{-2KT} \qquad \text{(Eq 18)}$$

Using Eq 16 and 18, the maximum stress and the minimum stress were then calculated as 638 MPa and 123 MPa, which is very close to the nominal stress level in the test (σ_{max} = 640 MPa and σ_{min} = 123 MPa). The elastic strain during fatigue can then be calculated easily by the equation:

$$\varepsilon_e = \sigma / E \qquad \text{(Eq 19)}$$

where ε_e is the elastic strain.

However, the inelastic strain of the specimen cannot be directly obtained from the original temperature profile because the mean temperature change is determined not only by the inelastic effect but also by the heat-conduction effect. Thus, the first step to calculate the inelastic strain will be to subtract the heat-conduction effect from the original temperature profile.

For each data point recorded in the fatigue test, the time interval, Δt, is 0.00483 s. If we consider $dt \approx \Delta t = 0.00483$ s, Eq 15 becomes:

$$dT_j = k \frac{1}{\Delta x^2 \rho C_p} (T_j - T_0) dt \qquad \text{(Eq 20)}$$

where *j* represents the *j*th experimental temperature data point, and dT_j is the temperature correction due to the heat-conduction effect for each fatigue data point.

Using Eq 20 to subtract the heat conduction effect from the original temperature profile, the temperature for each data point becomes:

$$T_{jc} = T_j + \sum_{n=1}^{j} dT_n \qquad \text{(Eq 21)}$$

where T_{jc} is the temperature after the subtraction of the heat-conduction effect.

The new back-calculated temperature profile without the heat-conduction effect (Fig. 9), is in contrast with Fig. 8, when

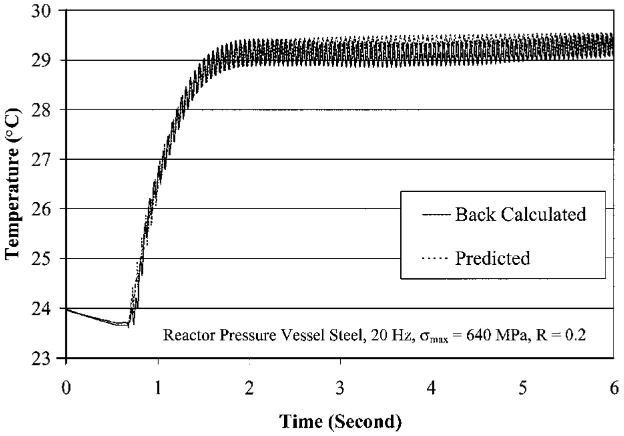

Fig. 9 Back-calculated and predicted temperature profiles without including the heat-conduction effect of reactor pressure vessel steel tested at 20 Hz, $\sigma_{\max}$ = 640 MPa, and R = 0.2

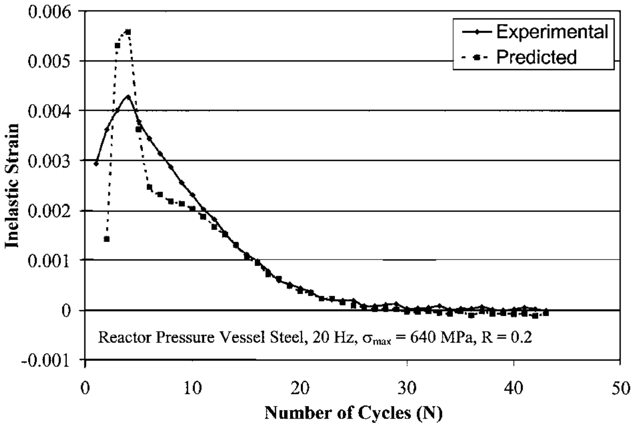

Fig. 10 Predicted and measured inelastic strain versus number of cycles profiles of reactor pressure vessel steel tested at 20 Hz, $\sigma_{\max}$ = 640 MPa, and R = 0.2

the presence of the heat-conduction effect causes the decrease of the temperature following the attainment of the maximum temperature, as mentioned before. In Fig. 9, the solid line is the back-calculated temperature profile without including the heat-conduction effect, while the dashed line is the predicted temperature profile using the stress-strain data before the heat-conduction correction. From the figure, the back-calculated temperature profile is in good agreement with the theoretical prediction.

The subtraction of two adjacent peak temperatures of each fatigue cycle can be directly related to the heat generated during each fatigue cycle. Then, Eq 11 can be rewritten as follows:

$$\rho C_p(T_{k+1} - T_k) = \int_{\varepsilon_{\min}}^{\varepsilon_{\max}} \sigma_u d\varepsilon - \int_{\varepsilon_{\min}}^{\varepsilon_{\max}} \sigma_l d\varepsilon = A_k \approx \sigma_{\max} \times \varepsilon_{in_k} \quad \text{(Eq 22)}$$

Where k represents the kth cycle, T_k is the peak temperature of the kth cycle, A_k is the area of the hysteresis loop of the kth cycle, and ε_{in_k} is the inelastic strain of the kth cycle.

Thus, the inelastic strain that is generated in each hysteresis loop can be calculated by:

$$\varepsilon_{in_k} = \frac{\rho C_p(T_{k+1} - T_k)}{\sigma_{\max}} \quad \text{(Eq 23)}$$

Figure 10 represents the measured and predicted inelastic strain changes during fatigue testing. The solid line is the experimental results, whereas the dashed line shows the predicted results. The experimental and predicted results are in reasonably good agreement. However, since the temperature for the first two cycles does not meet the theoretical model well (Fig. 8), and the real stress was not very stable for the first 10 cycles, which has been discussed before, the predicted data do not fit the experimental data well for the first several cycles. However, after 10 cycles, both curves match each other well. And the trends of the two curves are similar: for the first 4 cycles, the inelastic strain increases due to the yielding phenomenon; after 4 cycles, the inelastic strain decreases, material is strain hardening. Thus, the temperature profile appears to be able to be used to predict the inelastic behavior during fatigue in light of the back-calculation scheme.

5. Conclusion

A high-speed and high-sensitivity thermographic IR detection system has been applied to investigate the relationship between the temperature evolutions and fatigue behavior of RPV steels during 20 Hz and 1000 Hz fatigue testing. The temperature profiles during fatigue can be divided into five stages (Fig. 11): (1) an initial temperature increase due to the yielding phenomenon and plastic deformation; (2) the temperature decrease resulting from the heat-conduction effect; (3) a constant temperature region owing to the equilibrium between the material and the environment; (4) an abrupt increase resulting from the large plastic deformation and stress concentration at the tip of a macrocrack; and (5) a final drop due to the separation of the specimen. The constant temperature region during the 1000 Hz fatigue test can reach above 95 °C, relative to approximately 25 °C at 20 Hz. The much higher temperature could contribute to a shorter fatigue life at 1000 Hz than 20 Hz.

The temperature variations during fatigue can be modeled by incorporating three factors: (1) thermoelastic effect, (2) inelastic effect, and (3) heat-conduction effect. In a fatigue test without the applied heat source, the oscillation of temperature during fatigue can be explained by the thermoelastic effect, while the increase in the mean temperature is mainly caused by the inelastic effect with the consideration of heat conduction. A theoretical model has been developed to simulate the temperature profiles during fatigue. Moreover, the model can be used to back-calculate the stress-strain state from the experimental temperature profiles. The predicted results were found to be in good agreement with the experimental data. Above all, using the temperature profile to back calculate the stress-strain state provides a new method of analyzing and investigating the fatigue behavior of a material by simply monitoring its temperature evolutions.

I. **Initial temperature increase:**
- **Thermoelastic effect**
- **Inelastic effects**
  - **Yielding phenomenon**
  - **Plastic deformation**
  - **Internal friction**
  - **etc.**

II. **Temperature decrease:**
- **Thermoelastic effect**
- **Heat-conduction effect**

III. **Equilibrium state:**
- **Thermal equilibrium with the environment**
- **Thermoelastic effect**

IV. **Abrupt increase:**
- **Thermoelastic effect**
- **Inelastic effects**
  - **Plastic deformation**
  - **Internal friction**
  - **etc.**
- **Stress concentration**
- **Crack initiation and propagation**

V. **Final Drop:**
- **Specimen failure**

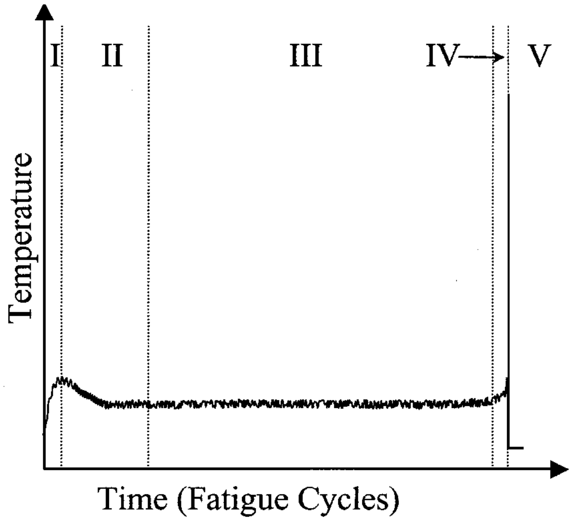

Fig. 11 Schematic of temperature changes during a fatigue test

Acknowledgments

I would like to thank my advisor, Prof. Peter Liaw, for his greatest help to me with theory and experiments. Also, I thank Dr. Hsing Wang from the Oak Ridge National Laboratory, Mr. Liang Jiang and Mr. Robert Odyseus from the University of Tennessee, Mr. J.Y. Huang, and Dr. R.C. Kuo from the Institute of Nuclear Energy Research (INER), and Dr. J.G. Huang from the Taiwan Power Company for their encouragement and help on my research. This project is supported by the Taiwan Power Company. We are also very grateful for the financial support of the National Science Foundation (DMI-9724476 and EEC-9527527) with Dr. D.R. Durham and Ms. M.F. Poats, as contract monitors. A portion of the work was sponsored by the U.S. Department of Energy, Secretary for Energy Efficiency and Renewable Energy, Office of Transportation Technologies, as part of the High Temperature Materials Laboratory User Program under contract DE-AC05-96OR22464, managed by the Lockheed Martin Energy Research Corporation.

References

1. S. Suresh: *Fatigue of Materials,* 2nd ed., Cambridge University Press, Cambridge, UK, 1998.
2. W.A. Logsdon, P.K. Liaw, and J.A. Begley: "Fatigue Crack Growth Behavior of Pressure Vessel Steels and Submerged Arc Weldments in a High-Temperature Pressurized Water Environment," ASTM STP 969, 1988, pp. 830-67.
3. P.K. Liaw, W.A. Logsdon, and J.A. Begley: "Fatigue Crack Growth Behavior of Pressure Vessel Steels and Submerged Arc Weldments in a High-Temperature Pressurized Water Environment," *Metall. Trans.,* 1989, *20A,* pp. 2069-85.
4. P.K. Liaw and W.A. Logsdon: "The Influence of Load Ratio and Temperature on the Near-Threshold Fatigue Crack Growth Rate Properties of Pressure Vessel Steels," *J. Eng. Mater. Tech.,* ASME, 1985, *107,* pp. 26-33.
5. P.K. Liaw, C.Y. Yang, S.S. Palusamy, and W. Ren: " Fatigue Crack Initiation and Propagation Behavior of Pressure Vessel Steels," *Eng. Fracture Mech.,* 1997, *57,* pp. 85-104.
6. W.A. Logsdon and P.K. Liaw: "Fatigue Crack Growth Rate Properties of SA508 and SA533 Pressure Vessel Steels and Submerged Arc Weldments in Room and Elevated Temperature Air Environments," *Eng. Fracture Mech.,* 1985, *22,* pp. 509-26.
7. J.Y. Huang, C.Y. Chen, K.F. Chien, R.C. Kuo, P.K. Liaw, and J.G. Huang: "Fatigue Behavior of Reactor Pressure Vessel Steels," *Proc. of Julia Weertman Symp., Minerals, Metals, and Materials Society (TMS) Fall Meeting,* Y.W. Chung, D. Dunand, P.K. Liaw, and G. Olson, ed., Cincinnati, OH, 31 Oct-4 Nov 1999, pp. 373-84.
8. J.Y. Huang, R.Z. Li, K.F. Chien, R.C. Kuo, P.K. Liaw, B. Yang, and J.G. Huang: "Fatigue Behavior of SA533-B1 Steels" in *Fatigue Fracture Mechanics,* 32nd Vol., STP 1406, R. Chona, ed., ASTM, West Conshohocken, PA, 2001, pp. 105-21.
9. L. Jiang, M. Huang, C.R. Brooks, and P.K. Liaw: "Acoustic Emission Detection of Fatigue Damage," *Proc. Nondestructive Evaluation (NDE) and Materials Properties IV Symp., TMS Annual Meeting,* P.K. Liaw, R.J. Arsenault, R.E. Green, Jr., K.L. Murty, and R.B. Thompson, ed., San Diego, CA, 28 Feb-4 Mar, 1999, pp. 43-60.
10. M.E. Fine, Z.M. Connor, and J.D. Achenbach: "Early Stages of Fatigue Damage in Riveted Alclad 2024-T3 Aluminum Alloy Lap Joint Specimens," *Proc. Nondestructive Evaluation (NDE) and Materials Properties IV Symp., TMS Annual Meeting,* P.K. Liaw, R.J. Arsenault, R.E. Green, Jr., K.L. Murty, and R.B. Thompson, ed., San Diego, CA, 28 Feb-4 Mar, 1999, pp. 1-9.
11. G. Birnbaum and G. Free: "Eddy-Current Characterization of Materials and Structures," *Symposium Sponsored by ASTM Committee E-7 on Nondestructive Testing,* American Society for Testing and Materials, Gaithersburg, MD, 5-7 Sept 1979.
12. A.A. Moss and H.I. Goldberg: *Computed Tomography, Ultrasound and X-ray: An Integrated Approach,* Masson Publication, NY, 1979.
13. M.P. Luong: "Fatigue Limit Evaluation of Metals Using an Infrared Thermographic Technique," *Mech. Mater.,* 1998, *28*(1-4), pp. 155-63.
14. K.S. Hermanson and B.I. Sandor: "Corrosion Fatigue Modeling via Differential Infrared Thermography," *Exp. Tech.,* 1998, *22*(3), pp. 19-21.
15. X. Tung, D. Wang, and H. Xu: "Heat Energy Dissipation in Fatigue Damage Process of Materials," *Acta Metall. Sinica (China),* 1992, *28*(4), pp. 163-69.
16. D. Zhang and B.I. Sandor: "Damage Evaluation in Composite Materials Using Thermoplastic Stress Analysis," ASTM STP 1122, 1991, pp. 341-53.
17. P.K. Liaw, R.J. Arsenault, R.E. Green, Jr., K.L. Murty, and R.B. Thompson, ed.: "Symp. Nondestructive Evaluation (NDE) and Materials Properties IV, TMS Annual Meeting," San Diego, CA, 28 Feb-4 Mar, 1999.

18. I. Todhunter and K. Pearson: *A History of the Elasticity and Strength of Materials,* Vol. 2, Cambridge University Press, Cambridge, UK, 1893.
19. M.A. Biot: "Thermoelasticity and Irreversible Thermodynamics," *J. Appl. Phys.,* 1956, *27*(3), pp. 240-53.
20. R. Rocca and M.B. Bever: "The Thermoelastic Effect in Iron and Nickel as a Function of Temperature," *Trans. Am. Instit. Mech. Eng.,* 1950, *188,* pp. 327-33.
21. D.H. Allen and W.E. Haisler: "A Theory For Analysis of Thermoplastic Materials," *Mech. Struct.,* 1981, *13,* pp. 129-35.
22. E.G. Henneke, K.L. Reifsnider, and W.W. Strinchcomb: "Thermography—NDI Method for Damage Detection," *J. Met.,* 1979, *31,* pp. 11-15.
23. R.H. Blanc and E. Giacometti, "Infrared Radiometry Study of the Thermomechanical Behavior of Materials and Structures" in *1st Int. Conf. of Stress Analysis by Thermoelastic Technics,* Sira Ltd., London, UK, Nov 1984.
24. B. Nayroles, R. Bouc, H. Caumon, J.C. Chezeaux, and E. Giacometti: "Infrared Telethermography and Structural Mechanics," *Int. J. Eng. Sci.,* 1981, *19,* pp. 929-47.
25. D.T. Lohr, N.F. Enke, and B.I. Sandor: "Analysis of Fatigue Damage Evolution by Differential Infrared Thermography," in *Dynamic Failure, Proc. 1987 SEM Fall Conference,* Savannah, GA, 25-27 Oct, 1987, pp. 169-74.
26. P.K. Liaw, H. Wang, L. Jiang, B. Yang, J.Y. Huang, R.C. Kuo, and J.G. Huang: "Thermographic Detection of Fatigue Damage of Pressure Vessel Steels at 1,000 Hz and 20 Hz," *Scripta Mater.,* 2000, *42,* pp. 389-95.
27. H. Wang, L. Jiang, P.K. Liaw, C.R. Brooks, and D.L. Klarstrom: "Infrared Temperature Mapping of ULTIMET Alloy During High-Cycle Fatigue Tests," *Metall. Mater. Trans. A,* 2000, *31,* pp. 1307-10.
28. M.P. Luong: "Short-Time Measurement of Fatigue Limit of Metals Using Infrared Thermography," *Rev. Métall. Cah. Inf. Tech.,* 1995, *92*(2), pp. 203-12.
29. J.M. Morgon and W.W. Millison: "A 1 kHz Servohydraulic Fatigue Testing System," in *Symp. Proc. in Honor of Professor Paul C. Paris, TMS Fall Meeting,* W.O. Soboyejo and T.S. Srivatsan, ed., Indianapolis, IN, 14-18 Sept 1997, pp. 305-12.
30. L. Jiang, H. Wang, P.K. Liaw, C.R. Brooks, and D.L. Klarstrom: "Characterization of the Temperature Evolution During High-Cycle Fatigue of the ULTIMET Superalloy: Experiment and Theoretical Modeling," *Metall. Mater. Trans. A,* 2001, *32*(9), pp. 2279-96.
31. B. Yang, P.K. Liaw, H. Wang, L. Jiang, J.Y. Huang, R.C. Kuo, and J.G. Huang: "Thermographic Investigation of The Fatigue Behavior of Reactor Pressure Vessel Steels," *Mater. Sci. Eng. A,* 2001, *314,* pp. 131-39.